Supplementary Information for
Global strain-induced scalar potential in graphene devices

Lujun Wang,[1,2,*] Andreas Baumgartner,[1,2] Péter Makk,[1,3] Simon Zihlmann,[1] Blesson S. Varghese,[1] David I. Indolese,[1] Kenji Watanabe,[4] Takashi Taniguchi,[5] and Christian Schönenberger[1,2]

[1]*Department of Physics, University of Basel, Klingelbergstrasse 82, CH-4056 Basel, Switzerland*

[2]*Swiss Nanoscience Institute, University of Basel, Klingelbergstrasse 82, CH-4056 Basel, Switzerland*

[3]*Department of Physics, Budapest University of Technology and Economics and Nanoelectronics Momentum Research Group of the Hungarian Academy of Sciences, Budafoki ut 8, 1111 Budapest, Hungary*

[4]*Research Center for Functional Materials, National Institute for Material Science, 1-1 Namiki, Tsukuba, 305-0044, Japan*

[5]*International Center for Materials Nanoarchitectonics, National Institute for Materials Science, 1-1 Namiki, Tsukuba 305-0044, Japan*

Supplementary Note 1. Energy level alignment diagram

The energy level diagram of a graphene electronic device at a gate voltage V_g is shown in Supplementary Fig. 1, where the band alignment between the metallic gate and the graphene connected to the grounded reservoirs is given by $E_F^{(M)} - E_F^{(G)} = -eV_g$, with $E_F^{(G)}$ and $E_F^{(M)}$ the Fermi levels of the graphene and the metallic gate, respectively. Since the graphene is grounded via the metallic contacts, $E_F^{(G)}$ is fixed throughout the measurements. The work function (WF) difference between the metallic gate (W_M) and undoped graphene (W_G^0) results in an electrostatic potential difference ϕ with a corresponding charge carrier density in the graphene. Due to the low density of states in graphene, one also needs to take into account the corresponding kinetic energies in the form of a finite chemical potential μ_{ch}, where E_D labels the Dirac point energy. Charged impurities in the surrounding, e.g. trapped charges in the dielectrics or adsorbed molecules nearby, induce an additional offset of the graphene WF, which we term ΔW_a [1, 2]. This offset then leads to a modification of μ_{ch}. In the end, the actual WF of the graphene (W_G) in the device is $W_G = \Delta W_a + W_G^0 - \mu_{ch}$. For the unstrained case, the fundamental relation between the relevant quantities can be directly found from Supplementary Fig. 1:

$$\begin{aligned} W_M - eV_g &= W_G - e\phi \\ &= (\Delta W_a + W_G^0 - \mu_{ch}) - e\phi. \end{aligned} \tag{1}$$

For tensile strain, the effect of the scalar potential is shown in Supplementary Fig. 1(b) (shaded in green), where we label the resulting changed quantities by symbols with a tilde and assume that W_M is a constant (due to the very large density of states in metals) and ΔW_a is not affected by strain. The strain-induced scalar potential shifts the Dirac point energy, leading to an increase in the intrinsic WF of undoped graphene, from W_G^0 to $\widetilde{W}_G^0$. This change has two effects in the device at a given gate voltage: a shift in the electrostatic potential difference, and a shift in the chemical potential. This results in a change in the charge carrier density, which can be detected in transport experiments. For the strained case at $\widetilde{V}_g$, the corresponding quantities in Supplementary Eq. 1 should be replaced by those with a tilde, leading to

$$\begin{aligned} W_M - e\widetilde{V}_g &= \widetilde{W}_G - e\widetilde{\phi} \\ &= (\Delta W_a + \widetilde{W}_G^0 - \widetilde{\mu}_{ch}) - e\widetilde{\phi}. \end{aligned} \tag{2}$$

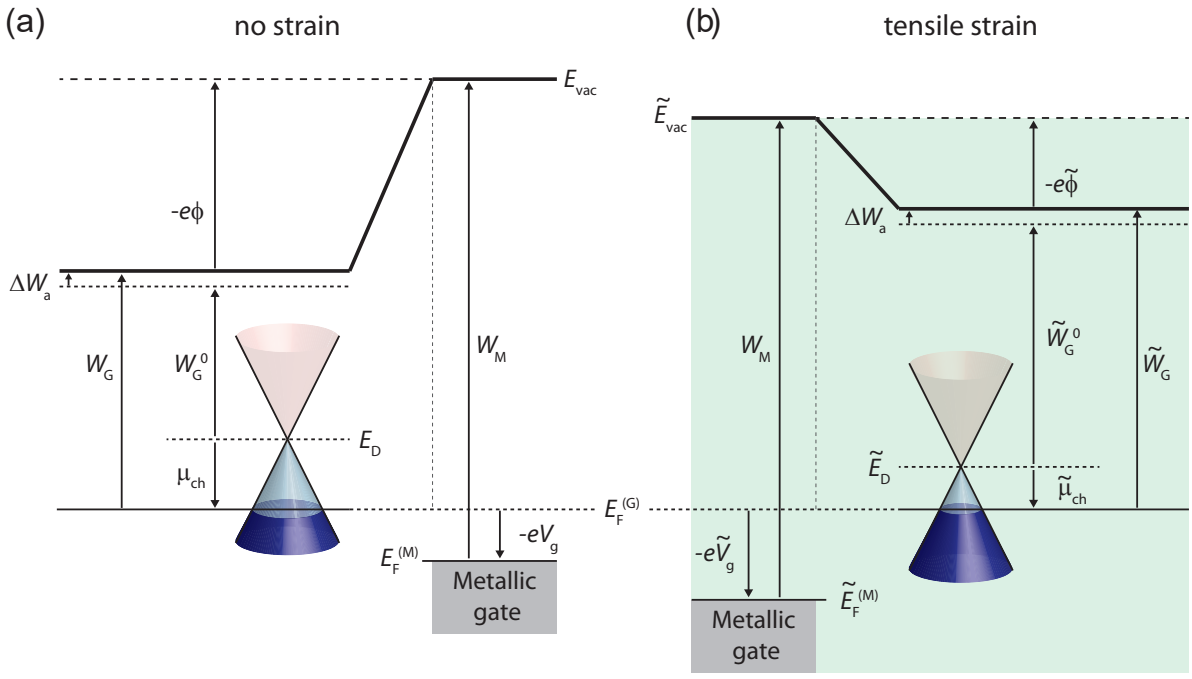

Supplementary Figure 1. Schematic energy level diagram of the device for **(a)** unstrained graphene at gate voltage V_g and for **(b)** strained graphene at gate voltage $\widetilde{V}_g$ (green shaded). The symbols are defined in the text. In our measurements, the graphene is grounded through the metallic contacts and therefore $E_F^{(G)}$ is fixed.

To extract the changes in intrinsic WF of undoped graphene induced by strain, and therefore the strain-induced scalar potential, we observe the evolution of a given conductance feature, which we assume to occur at a specific charge carrier density, n. A fixed n corresponds to a fixed chemical potential ($\mu_{ch} = \widetilde{\mu}_{ch}$) in the graphene and a fixed electrostatic potential difference ($\phi = \widetilde{\phi}$), assuming no changes in the gate capacitance by straining [3]. Under these conditions, the strain-induced scalar potential S can be directly extracted from Supplementary Eq. 1 and 2:

$$S = -(\widetilde{W}_G^0 - W_G^0) = e(\widetilde{V}_g^f - V_g^f), \tag{3}$$

where V_g^f and $\widetilde{V}_g^f$ are the gate voltages for a given conductance feature for the unstrained and strained cases, respectively. This directly demonstrates that all conductance features are shifted by the same amount in gate voltage for a given global homogeneous straining, as observed in the experiments in the main text.

Supplementary Note 2. Discussion of the conductance oscillations

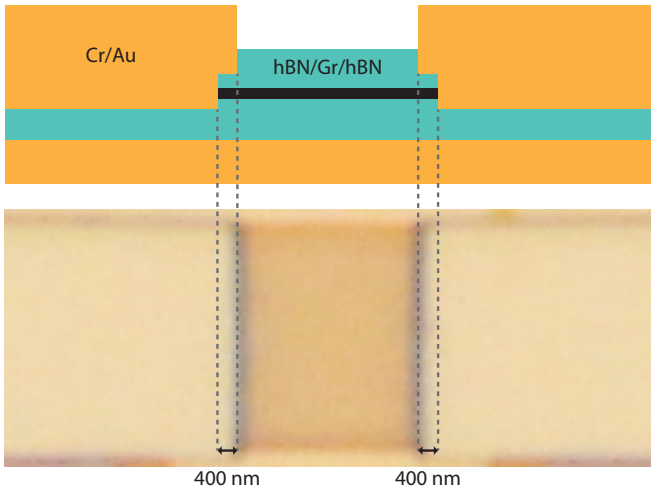

Supplementary Figure 2. Schematic cross section and optical microscope image of the device. The 400 nm overlap at each contact is intended for mechanical reinforcement.

Very regular oscillations in conductance are observed around the CNP, which stay unaffected by strain, as shown in Supplementary Fig. 3(b). These features are reminiscent of the quantized conductance originating from quantum point contacts [4, 5]. However, the corresponding Fermi wavelengths at the carrier densities of these oscillations are on the order of a few hundred nm, estimated with $\lambda_F = 2\pi/k_F = 2\pi/\sqrt{\pi n}$ and $n = \alpha(V_g - V_{CNP})$ with $\alpha \approx 4.9 \times 10^{15}\,\mathrm{m^{-2}\,V^{-1}}$, which are an order of magnitude smaller than the device width ($\sim$4.4 µm). Therefore, the possibility of the quantized channel conductance as the origin of these oscillations is ruled out. Another possibility could be the Fabry-Pérot resonances due to a region near each contact with a doping level different to the bulk of the device [6–9]. This is possible since the electrical contacts to the graphene are below the metallic leads and the overlap region is about 400 nm, as shown in Supplementary Fig. 2. This design is intended for mechanical reinforcement of the contacts [3]. From the conductance oscillations in the measurement, the cavity length L can be estimated with $L = \sqrt{\pi}/(\sqrt{n_{j+1}} - \sqrt{n_j})$, where $\sqrt{n_{j+1}}$ and $\sqrt{n_j}$ are the corresponding carrier densities of two consecutive oscillations [9]. A cavity length of $\sim$450 nm is extracted from our measurements, which matches well the $\sim$400 nm overlap near the contacts. We therefore tentatively attribute these oscillations to Fabry-Pérot resonances.

Supplementary Note 3. Reversibility

Here we present the measurements of the device shown in the main text for decreasing Δz at zero magnetic field. The two-terminal differential conductance G as a function of gate voltage V_g is shown in Supplementary Fig. 3(a) for different Δz. No significant changes can be seen on this scale. An enlargement of the CNP is shown in Supplementary Fig. 3(b), where the original $\Delta z = 0$ curve (black) is also added. With decreasing Δz, the curve gradually reverts back to the original position, which demonstrates the full reversibility of the strain-induced scalar potential.

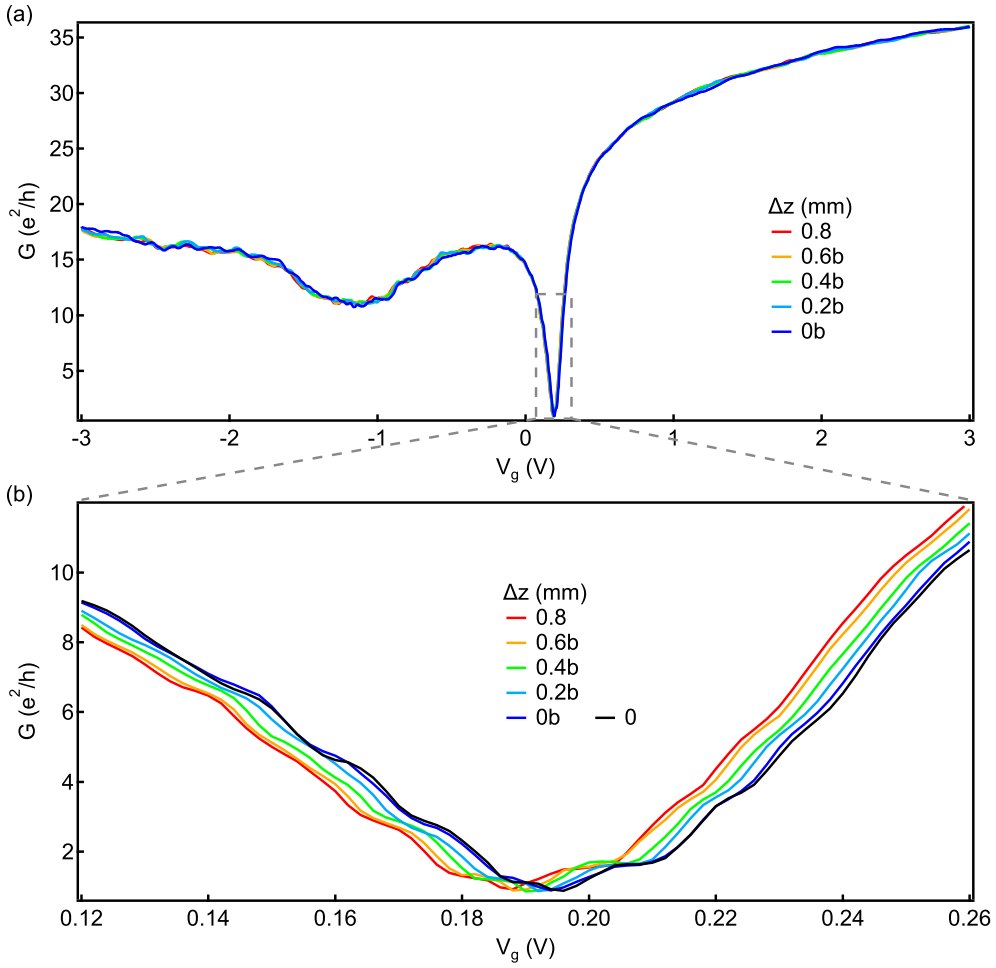

Supplementary Figure 3. **(a)** Two-terminal differential conductance G plotted as a function of gate voltage V_g for decreasing Δz. "b" stands for "backwards" in Δz. **(b)** Zoom-in to the CNP with the original $\Delta z = 0$ curve added as black.

Supplementary Note 4. Reversibility in quantum Hall regime

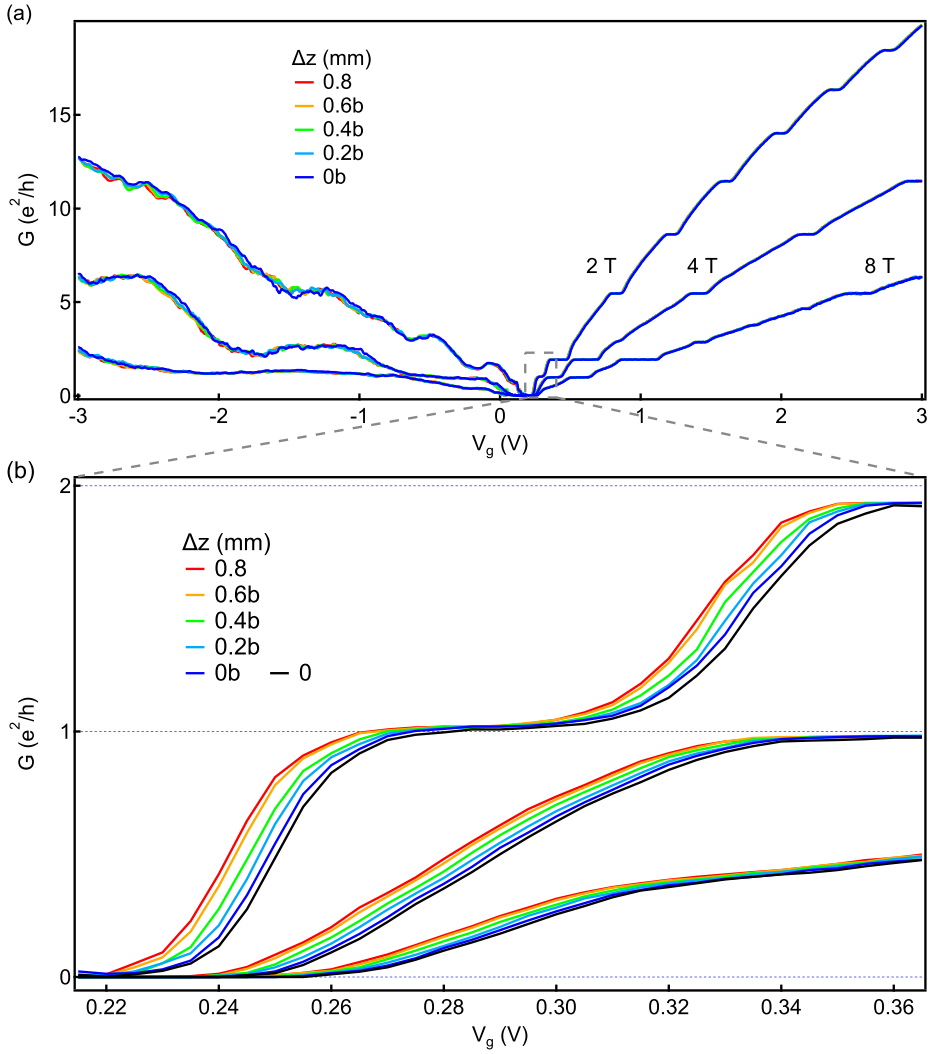

Supplementary Figure 4. **(a)** Two-terminal differential conductance G plotted as a function of the gate voltage V_g for decreasing Δz at $B = 2\,\mathrm{T}$, $4\,\mathrm{T}$ and $8\,\mathrm{T}$. "b" stands for "backwards" in Δz. **(b)** Zoom-in around the $\nu = 1$ quantum Hall plateau with the original $\Delta z = 0$ curve added as black.

Supplementary Fig. 4(a) shows the measured data from the same device as in the main text, but for decreasing strain values, at three different quantizing magnetic fields. No significant changes are found on this scale, except for the very left part. The quantum Hall plateaus in this region are not well developed due to a p-n junction forming near the contacts, which affects the electrical coupling of the graphene to the metallic contact. The changes observed here might be due to a small change in the effective contact resistance

with strain. An enlargement around the $\nu = 1$ plateau is shown in Supplementary Fig. 4(b), where the shift of the curves in gate voltage due to strain-induced scalar potential can be seen. The curve gradually reverts back with decreasing Δz, indicating the reversibility of the observed strain effect. The small mismatch between the $\Delta z = 0$(b) curve (blue) and the original $\Delta z = 0$ curve (black) can be attributed to a slight mechanical hysteresis of the bending setup.

Supplementary Note 5. Scalar potential in a second device

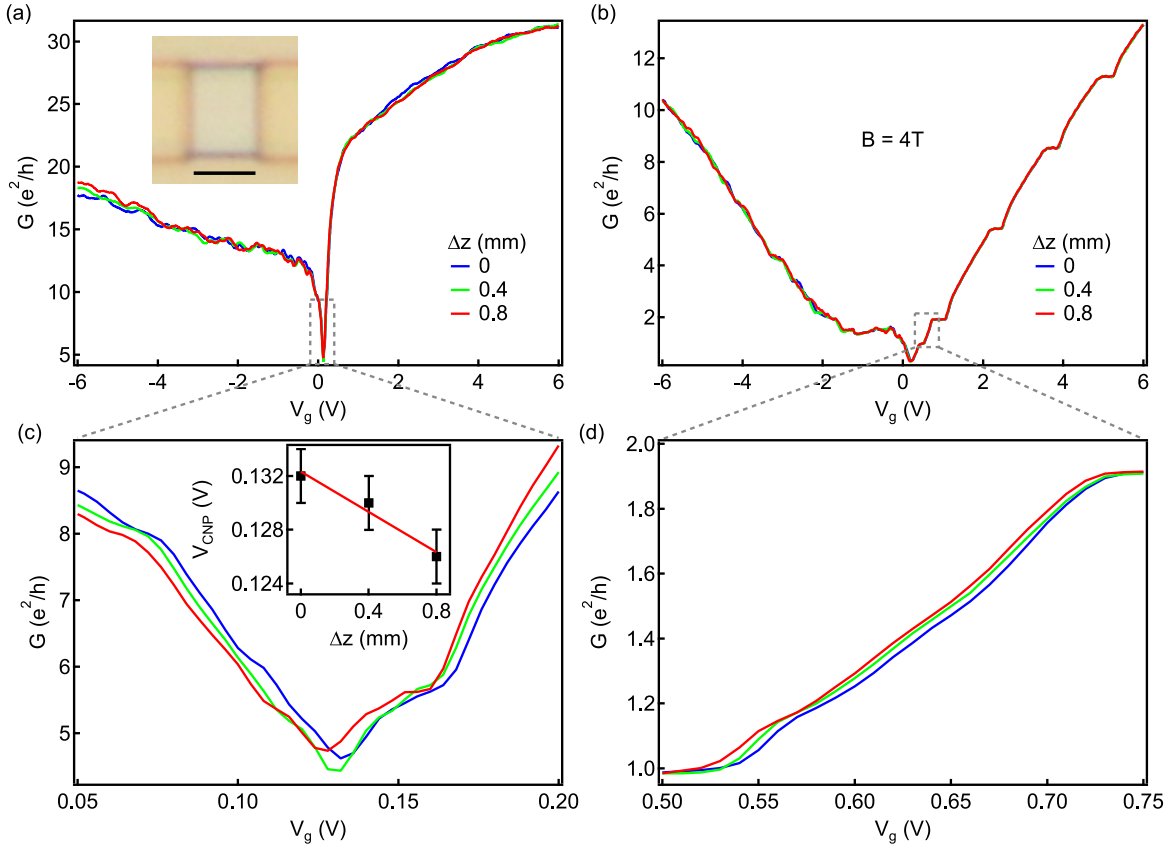

Supplementary Figure 5. Two-terminal differential conductance G plotted as a function of gate voltage V_g for different Δz at **(a)** $B = 0$ and **(b)** $B = 4\,\mathrm{T}$. The inset in **(a)** is an optical image of the measured device. Scale bar: 2 µm. The corresponding enlargements near the CNP are shown in **(c)** and **(d)**, respectively. The inset in **(c)** shows the position of the CNP (V_CNP) as a function of Δz. V_CNP is extracted as the gate voltage of minimum conductance. The error bars are estimated from half of the measurement step size in V_g. Red line is a linear fit with a slope of about $-7.5\,\mathrm{mV}$ per mm.

Here we present the data for a second device. The conductance curves without magnetic field and in the quantum Hall regime are plotted in Supplementary Fig. 5(a) and (b), respectively. On this scale, we can only observe changes with increasing Δz at large gate voltages, where the conductance is limited by the p-n junction near the contact, especially at the very left part of Supplementary Fig. 5(a). The changes seen in this region might be attributed

to a small change in the contact resistance, which does not affect the interpretation of the strain effect observed near the CNP, as shown in Supplementary Fig. 5(c) and (d). We note that the minimum conductance of this device is also slightly affected by strain, which might be attributed to a slight strain-induced change in the disorder potential. Other than that, a clear left-shift of the conductance curve with increasing Δz is observed. Using V_{CNP} as the reference point, a shift of $\sim$6 mV to the left in V_{g} is observed for $\Delta z = 0.8$ mm. A linear fit to the V_{CNP} as a function of Δz is shown in the inset of Supplementary Fig. 5(c), which results in a slope of about -7.5 mV per mm. This slope is slightly different from that of the device shown in the main text, which we attribute to the slightly different device geometry and layer thicknesses and the resulting different strain induced by the same displacement Δz of the wedge in the setup. The observed shift of the conductance curve with strain is consistent with the scalar potential interpretation.

Supplementary Note 6. Scalar potential in a device with opposite offset doping

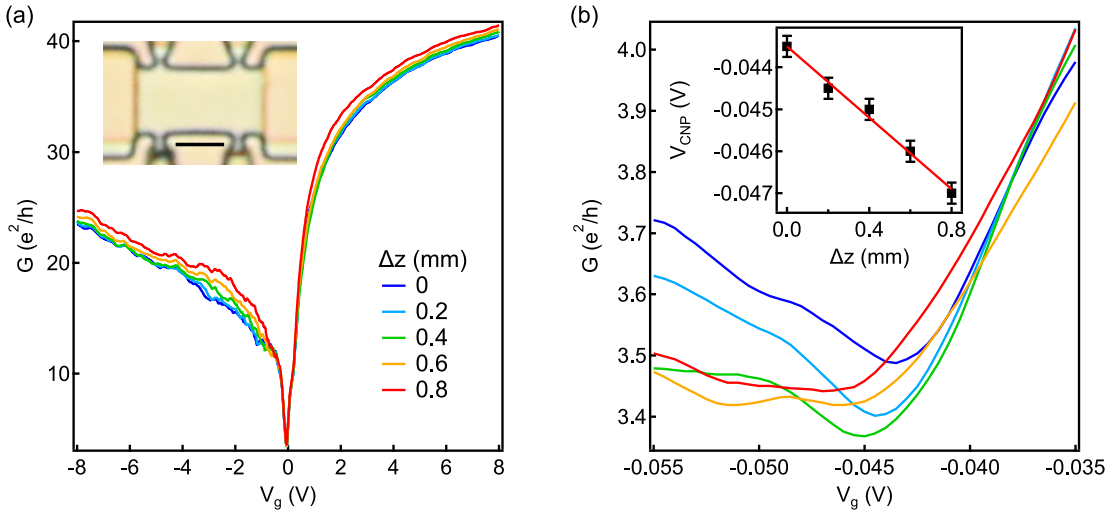

Supplementary Figure 6. **(a)** Two-terminal differential conductance G plotted as a function of gate voltage V_{g} for different Δz. The inset shows an optical image of the measured device. Scale bar: 2 µm. **(b)** Fine measurements of the same device near the CNP. The inset shows the position of the CNP (V_{CNP}) as a function of Δz. V_{CNP} is extracted as the gate voltage of minimum conductance. The error bars are estimated from half of the measurement step size in V_{g}. Red line is a linear fit with a slope of about -4.3 mV per mm.

To qualitatively demonstrate that the observed curve shifts in the main text are independent of the offset doping, we provide here experiments on a device with opposite offset doping. The two-terminal differential conductance of a third device as a function of V_g for different Δz are plotted in Supplementary Fig. 6(a). With increasing Δz, a mobility enhancement effect due to the in situ reduction of random strain fluctuations can be seen on this scale [10]. Measurements with a higher resolution near the CNP are shown in Supplementary Fig. 6(b). The minimum conductance of this device also changes with strain, which can be explained by the strain-induced changes in the disorder potential due to the relatively lower sample quality. We note that the other strain effects here might complicate the interpretation of the data. However, neither the mobility enhancement effect nor the minimum conductance change is expected to shift the CNP in gate voltage. Therefore, we can still use V_{CNP} as a reference point to extract the scalar potential effect. In Supplementary Fig. 6(b), a left-shift of V_{CNP} with increasing Δz is observed. The shift is best seen in the inset, where V_{CNP} is plotted as a function of Δz. A linear fit results in a slope of about $-4.3\,\mathrm{mV}$ per mm. The difference in this slope, compared to the other samples, mainly stems from the larger device size: in previous Raman studies we found that the strain induced at the same bending of the substrate roughly scales inversely with the device length between the clamped contacts [3]. Since this device is longer by a factor of ~ 2, we obtain a similar value for s_0 as for the device in the main text, for which we determine the strain levels from independent Raman experiments. Most importantly, in spite of the opposite sign of the offset doping in this device, the CNP is shifted in the same direction as in the other two discussed devices, which demonstrates that the observed effect is independent of the offset doping, supporting our picture of a strain-induced scalar potential.

* lujun.wang@unibas.ch

[1] G. Giovannetti, P. A. Khomyakov, G. Brocks, V. M. Karpan, J. van den Brink, and P. J. Kelly, Phys. Rev. Lett. **101**, 026803 (2008).

[2] Y.-J. Yu, Y. Zhao, S. Ryu, L. E. Brus, K. S. Kim, and P. Kim, Nano Lett. **9**, 3430 (2009).

[3] L. Wang, S. Zihlmann, A. Baumgartner, J. Overbeck, K. Watanabe, T. Taniguchi, P. Makk, and C. Schönenberger, Nano Lett. **19**, 4097 (2019).

[4] B. J. van Wees, H. van Houten, C. W. J. Beenakker, J. G. Williamson, L. P. Kouwenhoven, D. van der Marel, and C. T. Foxon, Phys. Rev. Lett. **60**, 848 (1988).

[5] B. Terrés, L. A. Chizhova, F. Libisch, J. Peiro, D. Jörger, S. Engels, A. Girschik, K. Watanabe, T. Taniguchi, S. V. Rotkin, J. Burgdörfer, and C. Stampfer, Nature Communications **7** (2016).

[6] A. F. Young and P. Kim, Nature Physics **5**, 222 (2009).

[7] P. Rickhaus, R. Maurand, M.-H. Liu, M. Weiss, K. Richter, and C. Schönenberger, Nature Communications **4** (2013).

[8] A. L. Grushina, D.-K. Ki, and A. F. Morpurgo, Applied Physics Letters **102**, 223102 (2013).

[9] C. Handschin, P. Makk, P. Rickhaus, M.-H. Liu, K. Watanabe, T. Taniguchi, K. Richter, and C. Schönenberger, Nano Lett. **17**, 328 (2017).

[10] L. Wang, P. Makk, S. Zihlmann, A. Baumgartner, D. I. Indolese, K. Watanabe, T. Taniguchi, and C. Schönenberger, Phys. Rev. Lett. **124**, 157701 (2020).